

Model Predictive and Reinforcement Learning Methods for Active Flow Control of an Airfoil with Dual-point Excitation of Plasma Actuators

AmirHossein Ghaemi^a, Abbas Ebrahimi^b, Majid Hajipour^c, Seyyed Mohammad Mahdy Shobeiry^b, Arash Fath Lipaei^b

^a*Faculty of Aerospace Engineering, Delft University of Technology, Kluyverweg 1, Delft, 2629 HS, Netherlands*

^b*Department of Aerospace Engineering, Sharif University of Technology, Azadi Ave., Tehran, 1458889694, Iran*

^c*College of Interdisciplinary Science and Technology, University of Tehran, Northern Kargar St., Tehran, 1439957131, Iran*

Abstract

This paper presents an analysis of Model Predictive Control (MPC) and Reinforcement Learning (RL) approaches for active flow control over a NACA (National Advisory Committee for Aeronautics) 4412 airfoil around the static stall condition at a Reynolds number of 4×10^5 . The Reynolds Averaged Navier-Stokes (RANS) equations with the Scale-Adaptive Simulation (SAS) turbulence model are utilized for the numerical simulations. The dielectric barrier discharge (DBD) plasma actuators were employed in dual excitation mode for flow separation control. The study systematically evaluates adaptive MPC, temporal difference reinforcement learning (TDRL), and deep Q-learning (DQL) based on optimizing the excitation frequency and expediting the time to identify stable conditions. Moreover, an integrated approach that combines signal processing with DQL is examined. The results demonstrate that while MPC and RL significantly improve flow control, RL approaches offer superior adaptability and performance. In optimal conditions, a lift coefficient of around 1.619 was achieved within less than 2.5 seconds with an excitation frequency of 100 or 200 Hz. This research highlights that RL-based approaches could perform better in flow control applications than MPC.

Keywords: Closed-loop active flow control, DBD plasma actuators, Flow separation control, Model predictive control, Reinforcement learning

1. Introduction

Closed-loop flow control (CFC) methods have emerged as a promising solution for mitigating the adverse hydrodynamic and aerodynamic effects. These methods dynamically monitor and influence the flow field, based on feedback from real-time flow conditions by utilizing sensors and actuators [1, 2]. Implementing CFC methods provides more efficient and adaptable hydro/aerodynamic systems in various engineering fields. In aviation, CFC methods can enhance aircraft maneuverability, delay stall, and improve fuel efficiency [3]. The automotive industry also benefits from these techniques by reducing drag and improving vehicle stability [4]. A critical area where CFC methods demonstrate their value is in managing flow separation, a non-linear phenomenon characterized by the detachment of the boundary layer from the surface, leading to increased drag and reduced lift and aerodynamic efficiency. Thus, research in closed-loop flow separation control has increasingly centered on novel approaches to improve aerodynamic performance. In the following, some of the most relevant works are reviewed.

The CFC methods can be categorized into model-based and data-driven approaches. Model-based methods have greatly enhanced the development of flow control strategies. Proctor et al. [5] expanded dynamic mode decomposition (DMD) to incorporate control effects, resulting in precise input-output models for complex, high-dimensional systems, referred to as dynamic mode decomposition with control (DMDC). Addressing uncertainties in system identification, Dovetta et al. [6] presented a hybrid framework combining perturbative methods and Monte Carlo techniques, efficiently estimating the statistical properties of identified systems. Huang and Kim [7] tackled separated flows using a linear optimal control approach based on system identification, successfully reducing separation bubble size. Lastly, Obeid et al. [8] used the NARMAX identification technique and Proportional-Integral (PI) controller for closed-loop control of flow separation over a NACA 0015 airfoil, significantly improving the lift coefficient and showcasing advanced system identification methods.

Data-driven approaches and deep reinforcement learning (DRL) have recently attracted much attention in the study of flow separation control [9, 10]. Vignon et al. [11] provided an overview of DRL frameworks in active flow control, identifying limitations and future directions. Shimomura et al. [12] showed the effectiveness of a CFC system using a deep Q Network (DQN) on a NACA 0015 airfoil, achieving higher control gains accompanied by the

attached flow. A RL-based method for actuator selection was introduced by Paris et al. [13] to optimize control performance of laminar flow separation around an airfoil. Additionally, Vinuesa et al. [14] and Varela et al. [15] reviewed DRL applications in flow control, with the aim of highlighting the potential for drag reduction of wings and circular cylinders.

DRL has been successfully applied to Active Flow Control (AFC) in turbulent conditions, achieving a 30% drag reduction at Reynolds (Re) number of 1000 by reducing turbulent fluctuations and elongating the recirculation bubble [16]. In varying Re number flows around a square cylinder, DRL’s adaptability was demonstrated with drag reductions up to 47%, effectively suppressing vortex shedding across different Re values [17]. In the control of turbulent separation bubbles (TSB), DRL outperformed classical periodic forcing, achieving a 25.3% reduction in TSB length at friction Reynolds number of 180 [18]. At friction Reynolds number of 750, DRL continued to show superiority with an 8.9% reduction in TSB length, while offering smoother control strategies [19].

MPC and RL each have their distinct advantages and challenges. MPC excels at handling constraints effectively by utilizing online optimization, but it can be computationally intensive and challenging to implement. On the other hand, RL methods are well-suited for dynamic, nonlinear environments as they do not require an exact system model, can adapt through experience, and can be implemented online. However, RL typically demands large amounts of data, is sensitive to the design of the reward function and exploration strategy, and involves intricate tuning processes.

Despite considerable progress in flow control methods, the efficiency of CFC methods has not been well documented. Particularly, a significant gap persists in the comparative evaluation of model predictive and RL-based strategies for improving active flow separation control over airfoils using plasma actuators. The existing literature primarily focuses on individual control methods, reinforcement learning algorithms, or specific applications of plasma actuators. However, a comprehensive comparison of these advanced methods to determine their relative effectiveness and potential integration has not been extensively explored. The novelty of this study lies in its systematic comparison of model predictive control and RL-based approaches, including TDRL, DQL, and DQL integrated with signal processing for active flow separation control. This research seeks to offer a more comprehensive understanding of the strengths and weaknesses of each method to advance more effective and efficient flow control strategies.

The rest of the paper is structured as follows: the flow control actuator section introduces the concept of dual-point excitation using plasma actuators. The underlying computational framework, including the governing equations, plasma actuator model, computational grid, and numerical methods used, are explained in the computational procedure section. In the flow control algorithms section, the various algorithms are investigated: adaptive MPC, TDRL, DQL, and signal processing integrated with DQL, each described with their respective algorithms, governing equations, and code implementations. Finally, the Results and Discussion section presents a thorough analysis of the findings, highlighting the comparative performance of the different control strategies and discussing their implications for future research and practical applications.

2. Flow Control Actuator

Among different AFC devices, DBD plasma actuators have garnered significant attention in flow control applications. Their popularity stems from several key advantages, including being fully electric, the absence of moving parts, rapid response time, low weight, and relatively low power consumption [20, 21]. In the previous work of authors [22], the control of separated shear layers using DBD plasma actuators on a NACA 0015 airfoil was introduced. The findings highlighted the technique’s success in stall prevention and its positive impact on lift-to-drag ratios. Li et al. [23] employed plasma co-flow jets on a NACA 0025 airfoil, which significantly delayed flow separation through enhanced mixing shear layers. Samimy et al. [24] extended active flow control applications to high-speed flows using advancements in plasma actuators to manipulate Kelvin-Helmholtz instabilities. Additionally, Gross and Fasel [25] studied separation control on a NACA 643-618 airfoil using plasma pulsed vortex generator jets, demonstrating high efficiency through linear stability analysis.

DBD plasma actuators consist of two electrodes: one that is exposed to the air and another that is covered by a dielectric material. As illustrated schematically in Fig. 1a, the system of a typical DBD plasma actuator operates by applying an AC voltage to the electrodes. When the voltage reaches a sufficiently high amplitude, it ionizes the air above the enclosed electrode. The ionized air particles are then accelerated by the electric field, exerting a body force on the surrounding neutral air. This interaction ultimately results

in the generation of an induced airflow [26].

Controlling flow separation through plasma actuators, particularly by exciting the separated shear layer, is highly sensitive to the choice of excitation frequency. Research indicates that a free shear layer is most responsive to perturbations near its natural vortex shedding frequency, leading many studies to select frequencies within this range for optimal separation control [27, 28, 29]. However, some research favors higher excitation frequencies [12, 30]. Another critical factor is the location of actuation, typically applied near the leading edge or the suction-side separation point to influence the upper separated shear layer [31]. Ebrahimi and Hajipour [32] introduced the concept of dual-point excitation, as shown in Fig. 1b, where both the suction side and trailing-edge shear layers are simultaneously excited using DBD plasma actuators. This method harnesses the interaction between the two shear layers, offering superior control during static stall conditions by reducing the separation zone and minimizing aerodynamic load fluctuations.

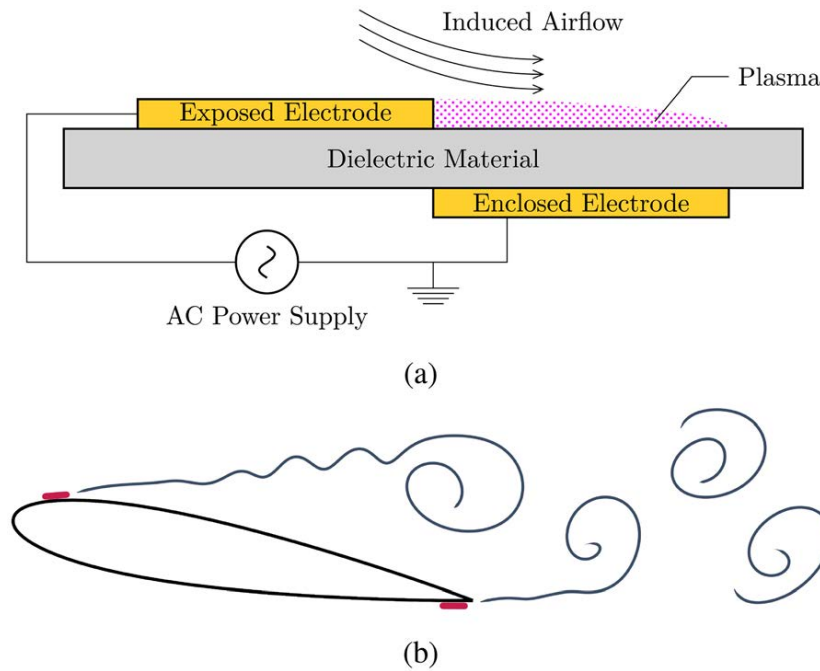


Figure 1: (a) Schematic of a DBD plasma actuator and (b) Schematic of dual-point excitation technique (actuators are indicated with red marks) [31].

3. Computational Procedure

3.1. Governing equations

The numerical flow simulations are performed by analyzing an incompressible viscous Newtonian fluid with constant properties. The governing equations employed for the Scale-Adaptive Simulation (SAS) turbulence model are based on the Reynolds-Averaged Navier-Stokes (RANS) equations, modified to include a scale-adaptive term that allows the model to transition between RANS and Large Eddy Simulation (LES) behavior based on the local flow conditions [33]. The continuity and momentum equations in Cartesian coordinates are:

$$\frac{\partial \rho}{\partial t} + \frac{\partial}{\partial x_i}(\rho u_i) = 0 \quad (1)$$

$$\frac{\partial}{\partial t}(\rho u_i) + \frac{\partial}{\partial x_j}(\rho u_i u_j) = -\frac{\partial P}{\partial x_i} + \frac{\partial \tau_{ij}}{\partial x_j} + \rho f_i \quad (2)$$

Herein, ρ is the fluid density, u_i is the velocity component in the i -th direction, P is the pressure, and τ_{ij} is the stress tensor which includes both molecular and turbulent contributions. The term ρf_i represents body forces, such as those due to plasma actuators. The stress tensor τ_{ij} is decomposed into the molecular viscosity part σ_{ij} and the Reynolds stress part τ_{ij}^T :

$$\sigma_{ij} = \mu \left(\frac{\partial u_i}{\partial x_j} + \frac{\partial u_j}{\partial x_i} \right) - \frac{2}{3} \mu \frac{\partial u_k}{\partial x_k} \delta_{ij} \quad (3)$$

$$\tau_{ij}^T = -\overline{\rho u'_i u'_j} \quad (4)$$

where μ is the dynamic viscosity of the fluid, and δ_{ij} is the Kronecker delta. The Reynolds stresses τ_{ij}^T are modeled using the SAS approach, which introduces an additional term to account for the resolved turbulent scales. In the SAS model, the additional source term S_{SAS} is incorporated into the turbulence model equations, to adaptively scale the turbulence production and dissipation based on the local flow features. This term enables the model to transition smoothly between RANS and LES behaviors, capturing a wider range of turbulent scales without the need for fine-tuning.

In this study, the SAS model adapts dynamically to the resolved turbulence scales, providing a more accurate and computationally efficient representation of the flow dynamics compared to traditional RANS models. This

approach ensures optimal performance in unsteady simulations, capturing essential flow features while reducing computational cost compared to full LES.

3.2. Plasma actuator model

In this study, the body force associated with plasma generation is derived from the phenomenological model introduced by Shyy et al. [34]. This model strikes a balance between simplicity and precision, making it ideal for studies on plasma actuator-based flow control [35, 36]. Shyy et al. [34] hypothesized that the plasma's electric field strength is linearly distributed within a triangular area directly downstream of the exposed electrode. Accordingly, the variation in field strength is calculated as:

$$|\vec{E}| = E_0 - k_1x - k_2y \quad (5)$$

E_0 represents the maximum electric field strength within the triangular region, and the constants k_1 and k_2 are determined to ensure that the field strength at the boundary between plasma and air (along the hypotenuse of the triangle) equals the breakdown value. Consequently, the body force within the plasma zone is given by:

$$\vec{F} = \rho_c e_c \vartheta \Delta T \vec{E} \quad (6)$$

The field vector \vec{E} is calculated as:

$$\vec{E} = \left(\frac{|\vec{E}|k_2}{\sqrt{k_1^2 + k_2^2}}, \frac{|\vec{E}|k_1}{\sqrt{k_1^2 + k_2^2}}, 0 \right) \quad (7)$$

where, ρ_c is the charge density of electrons, e_c is the elementary charge, ϑ is the frequency of the applied voltage, and ΔT is the discharge time.

In this research, the parameters of the plasma actuator are consistent with those used by Shyy et al. [34]. The exposed and enclosed electrode lengths are 0.5 mm and 3 mm, respectively. The height of the electrodes is 0.1 mm, and the gap between them in the streamwise direction is 0.25 mm, as illustrated schematically in Fig. 2. The applied voltage is 9 kV (root mean square), with a frequency of 3 kHz. The numerical model of the DBD plasma actuator has been validated by comparing it with Shy et al. [34] work. They assumed that plasma actuators operate in a steady, continuous mode; thus, the body force is modulated based on the duty cycle and excitation

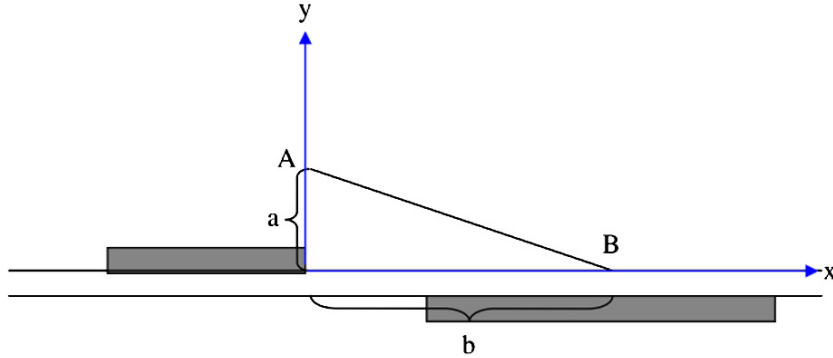


Figure 2: Triangular zone associated with plasma formation [32].

frequency to simulate unsteady actions. In this research, a duty cycle of 50% and excitation frequencies ranging from $f = 0$ to 400 Hz, corresponding to a normalized frequency of $F^+ = \frac{f \cdot c}{U_\infty}$ in the range of 0 to 11, are employed.

3.3. Computational grid

The computational test case is based on a NACA 4412 airfoil with a chord length $c = 0.4$ m, an angle of attack $\alpha = 15^\circ$, and a Reynolds number $Re = 4.0 \times 10^5$. As depicted in Fig. 3, the computational domain extends $20c$ downstream, $12.5c$ upstream and $12.5c$ in the direction normal to the chord. The airfoil surface is modeled as an adiabatic wall with a no-slip boundary condition. A freestream with a constant velocity of 14.6 m/s enters the domain from the upstream and bottom boundaries, while the downstream and top boundaries are defined as pressure outlets with ambient pressure.

A structured C-type grid was employed to simulate the flow. The numerical grid consists of 471800 Quadrilateral cells, with 365 computational nodes on the airfoil's suction side and 280 nodes on the pressure side. The normal distance of the nearest node to the airfoil surface is 1×10^{-5} m, ensuring that the near-wall y^+ is kept below 1. To accurately predict separation, a dense grid resolution is used around the airfoil's trailing edge (i.e., the wake region).

Following the previous work of authors [32], the novel concept of dual excitation technique is utilized to control the separated shear layers. Two plasma zones are implemented in the grid: one on the suction side of the airfoil just downstream of the separated shear layer, and the other on the pressure side at the airfoil's trailing edge. The dimensions of these zones are selected based on the work by Shy et al. [34], with the plasma body

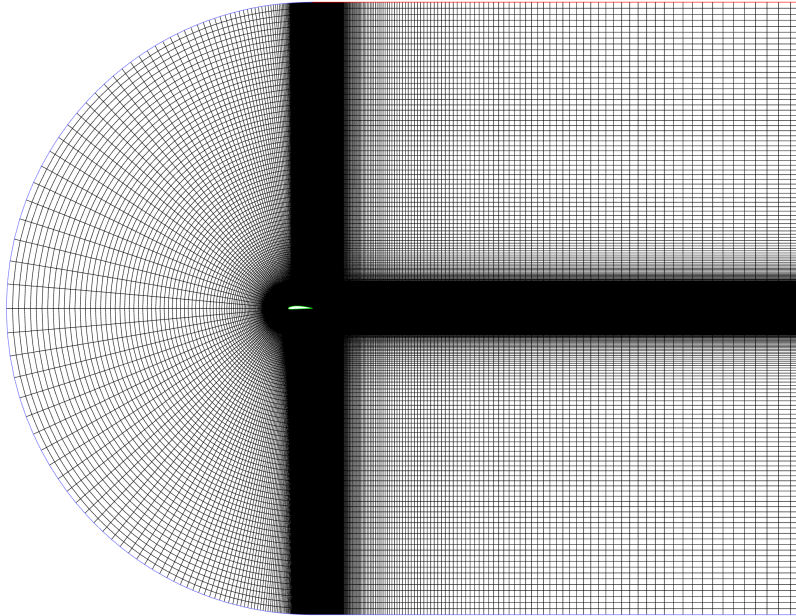


Figure 3: Side view of the computational domain.

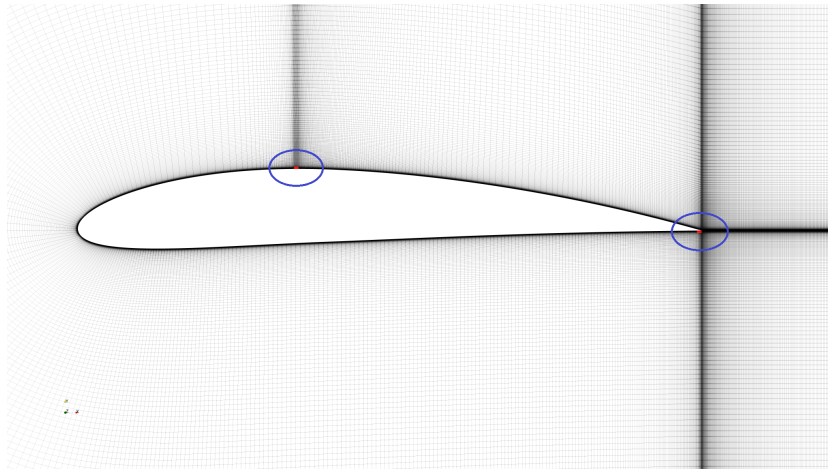


Figure 4: Detailed view of computational grid around airfoil and the plasma zones.

force applied only within these regions. The suction side actuator is located at $x = 0.35c$, while the pressure side actuator is positioned at $x = 0.99c$. The grid's streamwise resolution in the plasma zones is chosen carefully to

satisfy the accuracy requirements for predicting plasma wall jets and flow separation. Fig. 4 illustrates a detailed view of the plasma zones encircled in blue and computational grid around airfoil.

3.4. Numerical method

The computational fluid dynamics (CFD) simulations in this study were conducted using a pressure-based finite volume solver. The simulations were transient and performed in a two-dimensional planar space, with gravity effects neglected.

The air with constant properties, a density of 1.225 kg/m^3 and a viscosity of $1.7894 \times 10^{-5} \text{ kg/(m}\cdot\text{s)}$, was used in the simulation. A coupled scheme with Rhie-Chow momentum-based flux type [37] was implemented for pressure and velocity fields. To achieve high accuracy in the numerical solution, least squares cell-based gradient discretization was applied. Second-order discretization was used for pressure, while bounded central differencing was applied for momentum. Second-order upwind schemes were used for both turbulent kinetic energy and specific dissipation rate.

The transient nature of the flow was captured using a bounded second-order implicit scheme, which provides a balance between stability and accuracy for time-dependent simulations. This setup was carefully selected to provide a comprehensive and accurate representation of the flow dynamics over the airfoil with active flow control using plasma actuators.

4. Flow Control Algorithms

The efficiency of CFC techniques is significantly influenced by the underlying algorithms, as they directly impact the ability to optimize fluid flow behavior and achieve flow control objectives. In order to conduct a comparative analysis, this study evaluates Adaptive MPC and RL-based techniques based on their ability to optimize excitation frequency and expedite the identification of stable conditions. Approaches like MPC rely on deriving a dynamic model between input and output to predict and adjust flow parameters in real time, offering precise control based on the identified model accuracy. Recently, RL techniques such as temporal difference (TD) and DQL have emerged as powerful alternatives, capable of learning optimal control policies through environmental interaction and feedback, thus providing model-free solutions. Furthermore, integrating signal processing with

DQL provides advanced feature extraction from complex flow data, resulting in more effective and precise control strategies. This section delves into the various flow control algorithms, highlighting their underlying principles, advantages, and applications in fluid dynamics.

All the methods evaluated in this study are implemented in an online learning manner, where each technique trains while simultaneously providing outputs for the simulation, enabling real-time adaptation. For the RL-based methods, hyperparameters were determined after multiple initial runs. The selection of hyperparameters was based on the fact that the model initially explores its options and selects the optimal action as quickly as possible. In each model, the lift coefficient serves as the input, while the output is the actuation frequency. The action space for the RL-based methods is designed to be discrete, as the desired frequency value for flow control lies within the superharmonic frequencies of wake, specifically from $F^+ = 1$ to $F^+ = 6$. Frequencies beyond this range do not elicit an effective fluid response to excitation [12]. Moreover, the online learning approach involves significant computational demands, emphasizing the importance of using efficient, lightweight models to balance computational feasibility and control effectiveness. The authors explored more complex network architectures beyond those presented in this paper and found that increasing complexity led to a decline in performance.

4.1. Adaptive MPC

MPCs are renowned for their ability to control complex processes with great performance in energy optimization, robustness, stability, and disturbance rejection [38, 39, 40, 41]. This class of controllers requires a model to predict future plant outputs and then take actions to minimize future errors between desired values and actual outputs. In this section, we aim to design an adaptive Generalized Predictive Controller (GPC) that can fit a linear model between the control input $u(t)$ (i.e., actuator excitation frequency) and the plant output $y(t)$ (i.e., airfoil lift coefficient) using the Recursive Least Squares (RLS) system identification method.

The basic idea of GPC is to calculate a sequence of future control inputs in such a way that it minimizes a multistage cost function defined over a prediction horizon [42]. To do this, we first define a Controller Auto-Regressive Integrated Moving-Average (CARIMA or ARIMAX) model [43] for describing the GPC algorithm:

$$A(z^{-1})y(t) = B(z^{-1})u(t-1) + C(z^{-1})\frac{e(t)}{\Delta} \quad \text{with} \quad \Delta = 1 - z^{-1} \quad (8)$$

where $z = e^{sT_c}$ is a discrete-time equivalent of the Laplace variable s , and T_c is the controller time step. Also, $e(t)$ is zero-mean white noise and A, B, C are polynomials in the backward shift operator z^{-1} :

$$\begin{aligned} A(z^{-1}) &= 1 + a_1z^{-1} + a_2z^{-2} + \dots + a_{n_a}z^{-n_a} \\ B(z^{-1}) &= b_0 + b_1z^{-1} + b_2z^{-2} + \dots + b_{n_b}z^{-n_b} \\ C(z^{-1}) &= 1 + c_1z^{-1} + c_2z^{-2} + \dots + c_{n_c}z^{-n_c} \end{aligned} \quad (9)$$

In this study, we consider $C(z^{-1}) = 1$, meaning we have only white noise in our process. Due to the complexity of the problem, a system identification method is needed to estimate the A and B polynomials discussed in the system identification section. The GPC algorithm consists of applying a control sequence that minimizes a multistage cost function of the form:

$$J(N_p, N_u) = \sum_{j=1}^{N_p} (\hat{y}(t+j|t) - w(t+j))^2 + \sum_{j=1}^{N_u} \lambda(j) (\Delta u(t+j-1))^2 \quad (10)$$

where N_p is the maximum costing horizon, also known as the prediction horizon, and N_u is the control horizon. $\lambda(j)$ is a control-weighting sequence. Additionally, $\hat{y}(t+j|t)$ is an optimum j -step ahead prediction of the system output based on data up to time t and $w(t+j)$ is the future reference trajectory. This implies that in the GPC algorithm, an achievable desired value should be defined for the lift coefficient and used as $w(t)$ in the cost function. To derive the j -step ahead prediction of the system output $y(t+j)$ based on eq. (8), consider the following Diophantine equation:

$$1 = E_j(z^{-1})\tilde{A}(z^{-1}) + z^{-j}F_j(z^{-1}) \quad \text{with} \quad \tilde{A}(z^{-1}) = \Delta A(z^{-1}) \quad (11)$$

where polynomials E_j and F_j are uniquely defined for a given \tilde{A} that have degrees of $j-1$ and n_a , respectively. If eq. (8) is multiplied by $\Delta E_j(z^{-1})z^j$ and using eq. (11), we can find the j -step ahead prediction of the system output:

$$y(t+j) = G_j(z^{-1})\Delta u(t+j-1) + F_j(z^{-1})y(t) + E_j(z^{-1})e(t+j) \quad (12)$$

where $G_j(z^{-1}) = E_j(z^{-1})B(z^{-1})$. Thus, the degree of polynomial $E_j(z^{-1})$ equals $j-1$, the noise term $e(t+j)$ in equation eq. (12) is all in the future. Therefore the best prediction of $y(t+j)$ is:

$$\hat{y}(t+j|t) = G_j(z^{-1})\Delta u(t+j-1) + F_j(z^{-1})y(t) \quad (13)$$

Following from Ref. [43], it is simple to show that the required polynomials E_j and F_j in eq. (13) can be obtained recursively as:

$$\begin{aligned} E_j(z^{-1}) &= e_{j,0} + e_{j,1}z^{-1} + \dots + e_{j,j-1}z^{-(j-1)} \\ F_j(z^{-1}) &= f_{j,0} + f_{j,1}z^{-1} + \dots + f_{j,n_a}z^{-n_a} \end{aligned} \quad (14)$$

following the recursion algorithm:

$$\begin{aligned} E_1 &= 1; \quad F_1 = z \left(1 - \tilde{A}(z^{-1}) \right) \\ E_{j+1}(z^{-1}) &= E_j(z^{-1}) + f_{j,0}z^{-j} \\ f_{j+i} &= f_{j,i+1} - f_{j,0}\tilde{a}_{i+1} \quad (i = 0, 1, \dots, n_a - 1) \end{aligned} \quad (15)$$

also, G_{j+1} can be calculated recursively:

$$G_{j+1} = E_{j+1}B = (E_j + f_{j,0}z^{-j})B = G_j + f_{j,0}z^{-j}B \quad (16)$$

Considering eq. (13), we can write a set of j -ahead predictions:

$$\begin{aligned} \hat{y}(t+1|t) &= G_1\Delta u(t) + F_1y(t) \\ \hat{y}(t+2|t) &= G_2\Delta u(t+1) + F_2y(t) \\ &\vdots \\ \hat{y}(t+N_p|t) &= G_{N_p}\Delta u(t+N_p-1) + F_{N_p}y(t) \end{aligned} \quad (17)$$

which can be displayed in the following matrix form:

$$\hat{\mathbf{y}} = \mathbf{G}\mathbf{u} + \mathbf{f} \quad (18)$$

This form shows that the response of the system consists of two parts: forced response $\mathbf{G}\mathbf{u}$ and free response \mathbf{f} . Matrix \mathbf{G} and vectors $\hat{\mathbf{y}}$, \mathbf{u} , and \mathbf{f} in eq. (17) can be defined as follows:

$$\begin{aligned}
\mathbf{G} &= \begin{bmatrix} g_0 & 0 & \cdots & 0 \\ g_1 & g_0 & \cdots & 0 \\ \vdots & \vdots & \ddots & \vdots \\ \vdots & \vdots & \cdots & g_0 \\ \vdots & \vdots & \ddots & \vdots \\ g_{N_p-1} & g_{N_p-2} & \cdots & g_{N_p-N_u} \end{bmatrix} \\
\hat{\mathbf{y}} &= [\hat{y}(t+1|t), \hat{y}(t+2|t), \cdots, \hat{y}(t+N_p|t)]^T \\
\mathbf{u} &= [\Delta u(t), \Delta u(t+1), \cdots, \Delta u(t+N_u-1)]^T \\
\mathbf{f} &= [f(t+1), f(t+2), \cdots, f(t+N_p)]^T
\end{aligned} \tag{19}$$

with $f(t+i) = \left(G_i(z^{-1}) - \sum_{k=0}^{i-1} g_k z^{-k}\right) z^i \Delta u(t) + F_i(z^{-1})y(t)$ for $i = 1, \dots, N_p$ and considering $N_p \geq N_u$, which means that $\Delta u(t+i) = 0$ for $i \geq N_u$. Therefore, the cost function provided in eq. (10) can be rewritten in the following form:

$$\begin{aligned}
J &= (\mathbf{G}\mathbf{u} + \mathbf{f} - \mathbf{w})^T (\mathbf{G}\mathbf{u} + \mathbf{f} - \mathbf{w}) + \lambda \mathbf{u}^T \mathbf{u} \\
\mathbf{w} &= [w(t+1), w(t+2), \cdots, w(t+N_p)]^T
\end{aligned} \tag{20}$$

Assuming there are no constraints on future controls, the minimum of J can be found by making $\frac{\partial J}{\partial \mathbf{u}} = 0$, which leads to:

$$\mathbf{u} = (\mathbf{G}^T \mathbf{G} + \lambda I)^{-1} \mathbf{G}^T (\mathbf{w} - \mathbf{f}) \tag{21}$$

A system identification method is needed that can estimate polynomials A and B of the system to describe control input $u(t)$ and complete Adaptive GPC design. According to equation eq. (8), we can perform the RLS method [44] as follows:

$$\begin{aligned}
k(t) &= P(t-1)\phi(t) (I + \phi^T(t)P(t-1)\phi(t))^{-1} \\
P(t) &= (I - k(t)\phi^T(t)) P(t-1) \\
\theta(t) &= \theta(t-1) + k(t) (y(t) - \phi^T(t)\theta(t-1))
\end{aligned} \tag{22}$$

where the regressors vector $\phi(t)$ and parameters vector $\theta(t)$ are defined as follows:

$$\begin{aligned}\phi(t) &= [-y(t-1) \ \cdots \ -y(t-n_a) \ u(t-1) \ \cdots \ u(t-n_b)]^T \\ \theta(t) &= [a_1 \ \cdots \ a_{n_a} \ b_1 \ \cdots \ b_{n_b}]^T\end{aligned}\tag{23}$$

The system output $y(t)$ is the average of the lift coefficients from the last $\frac{\text{FoM} \times T_c}{\text{TimeStep}}$ intervals, calculated over each T_c , where FoM stands for Fraction of Mean and is set between 0 and 1.

The parameters required for implementing the Adaptive GPC algorithm are described in TABLE. 1. These parameters are used in the results.

Table 1: Parameter values for adaptive GPC algorithm.

Parameter	Value	Description
Input Range	[50, 400]	Range of the continuous control inputs (Hz)
FoM	0.25	Fraction of mean
λ	1	Control weight
n_a	5	Order of polynomial A
n_b	5	Order of polynomial B
N_p	11	Prediction horizon
N_u	7	Control horizon
T_c	0.1	Controller time step (s)
TimeStep	1e-4	Simulation time step (s)

4.2. TDRL

TDRL is a class of model-free methods used in reinforcement learning, where an agent learns to make decisions by interacting with an environment. Unlike traditional Monte Carlo methods that wait until the end of an episode to update value estimates, TD methods update estimates based on partially observed episodes, making them more efficient for online learning. TD learning combines ideas from Monte Carlo methods and dynamic programming. The core idea behind TD learning is to estimate the value function, which represents the expected return (future rewards) for being in a given state and following a particular policy. The TD learning algorithm iteratively updates the value estimates using the difference between the predicted value and the actual reward received, known as the TD error.

The reward is calculated based on the difference between the current mean lift coefficient ($C_{l_{\text{mean}}}$), which is the mean of the last $\frac{\text{FoM} \times T_c}{\text{TimeStep}}$ lift coefficients in

a Controller Time Step, and a baseline value, using an exponential function to emphasize larger improvements. The current state is assumed to be the previous reward. The Q-value for the selected action is updated as eq. (24) using the TD error, incorporating the immediate reward and the maximum future Q-values.

$$Q(s, a) \leftarrow Q(s, a) + \alpha \left(r + \gamma \max_{a'} Q(s', a') - Q(s, a) \right) \quad (24)$$

where, s is the current state from which the action a is taken, s' is the new state resulting from taking action a , α is the learning rate, r is the reward received after taking action a in state s , γ is the discount factor, $Q(s, a)$ is the current Q-value for taking action a in state s , and $\max_{a'} Q(s', a')$ is the maximum Q-value among all possible actions from the new state s' . The algorithm decides whether to explore new actions or exploit the current knowledge by comparing a random number with the exploration rate (ϵ). ϵ is decayed by multiplying it by exploration decay (κ) in every controller time step. The parameters required for implementing the TDRL algorithm are described in TABLE. 2.

Table 2: Parameter values for TD and DQL algorithms.

Parameter	TDRL value	DQL value	Description
Actions	0:50:400	0:50:400	Discrete action space
α	0.4	1×10^{-2}	Learning rate
BaseLine	1.44	1.44	Baseline lift coefficient
ϵ	0.9	0.9	Initial exploration rate
FoM	0.25	0.25	Fraction of mean
γ	0.9	0.25	Discount factor
κ	0.95	0.95	Exploration rate decay
T_c	0.1	0.1	Controller time step
TimeStep	1×10^{-4}	1×10^{-4}	Simulation time step

4.3. Deep Q - Learning

DQL is a model-free RL algorithm that combines Q-Learning with deep neural networks. It is designed to handle environments with high-dimensional state spaces where traditional Q-Learning would be infeasible [45]. DQL approximates the Q-value function using a neural network, which takes the

current state as input and outputs Q-values for each possible action. The algorithm iteratively updates the Q-values based on the observed rewards and transitions. Like the previous method, rewards and states are calculated based on the environment’s responses to the agent’s actions. The Q-value update rule is given by:

$$Q(s, a) \leftarrow Q(s, a) + \alpha \left[r + \gamma \max_{a'} Q(s', a') - Q(s, a) \right] \quad (25)$$

Where α is the learning rate that determines the extent to which the new information overrides the old information. If $\alpha = 1$, the equation simplifies to:

$$Q(s, a) \leftarrow r + \gamma \max_{a'} Q(s', a') \quad (26)$$

where, $Q(s, a)$ is the Q-value for taking action a in state s , r is the reward received after taking action a , $\max_{a'} Q(s', a')$ is the maximum predicted Q-value for the next state s' , considering all possible actions a' , and $Q(s', a')$ is the Q-value function approximator (neural network) used for predicting future rewards.

The ϵ -greedy policy is used to balance exploration and exploitation. The neural network used in DQL is designed to approximate the Q-value function. It takes the current state as input and outputs the Q-values for all possible actions. The architecture of the network in this implementation is as follows:

- **Input Layer:** A feature input layer with 1 input feature.
- **Hidden Layers:** Four fully connected layers, each with 4 neurons and ReLU activation functions. These layers allow the network to learn complex representations of the state-action space.
- **Output Layer:** A fully connected layer with the number of neurons equal to the number of possible actions. This layer outputs the Q-values for each action.

The network is trained using the Stochastic Gradient Descent with Momentum (SGDM) optimizer, with an initial learning rate of 0.01 and a maximum of 100 epochs, using half-mean-squared error as the loss function. This setup allows the network to learn the optimal Q-value function through iterative updates based on the observed rewards and transitions. The network architecture and the parameters required for implementing the DQL algorithm are described in Fig. 5 and Table 2, respectively.

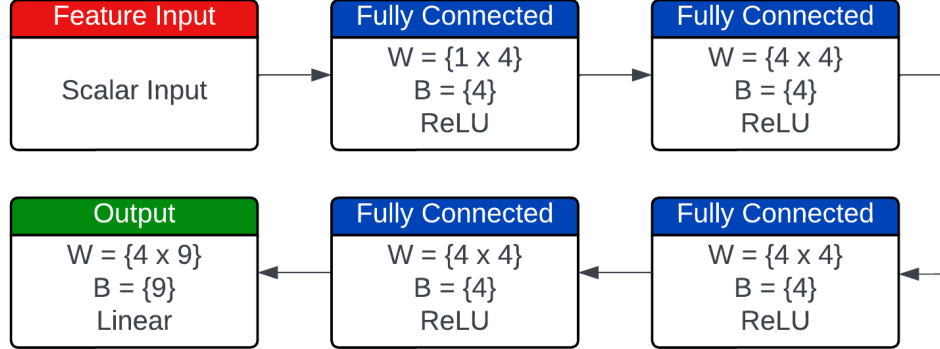


Figure 5: DQN Network Architecture. W and B indicate weight and Bias of layers, respectively.

4.4. Signal processing integrated with Deep Q-Learning

Signal processing integrated with DQN aims to enhance the algorithm’s ability to handle and interpret time-series data effectively. By incorporating Long Short-Term Memory (LSTM) [46] layers within the neural network architecture, the algorithm can better understand temporal dependencies and patterns in the data, leading to more informed decision-making. This approach is particularly useful in environments where the state information is derived from sequences of observations, such as time-series signals. The following describe the algorithm and the governing equations used in this integrated approach.

The neural network in this approach takes sequences of states as input and outputs Q-values for each possible action. The algorithm iteratively updates the Q-values based on the observed rewards and transitions, allowing the agent to learn optimal actions over time by recognizing patterns and dependencies in the sequential data. This integration of signal processing enhances the agent’s decision-making ability in dynamic environments.

As in the previous method, rewards and states are calculated based on the environment’s responses to the agent’s actions. The primary difference lies in the state representation, which is now a vector comprising the last $\frac{FoM \times T_c}{TimeStep}$ of lift coefficients over each controller time step. Despite this change in state and reward definitions, the governing equations, methodology, and ϵ -greedy policy and network training options remain identical to those used in the

prior approach. The parameters are identical to the previous method.

The neural network used in this implementation of Deep Q-Learning is

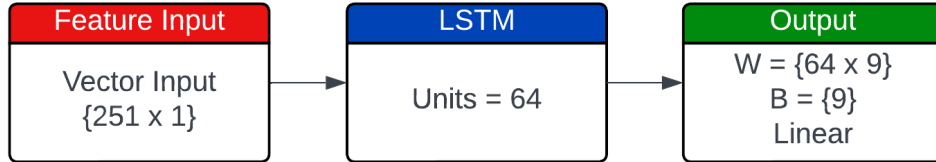


Figure 6: Signal processing integrated with DQL Network Architecture.

specifically designed to handle time-series data. It takes sequences of states as input and outputs the Q-values for all possible actions. The architecture of the network is structured as follows (see Fig. 6):

- **Input Layer:** A feature input layer with 251 input features.
- **LSTM Layer:** An LSTM (Long Short-Term Memory) layer with 64 neurons, designed to capture temporal dependencies in the data.
- **Fully Connected Layer:** A fully connected layer with the number of neurons equal to the number of possible actions, outputting the Q-values for each action.

5. Results and Discussion

This section presents the outcomes of different control strategies applied to the airfoil flow separation problem. The section begins with validating the baseline model using experimental results from wind tunnel tests of Mallor et al. [47] and Tabatabaei et al. [48]. After the baseline is established, the performance of adaptive MPC is analyzed and these results are compared with those obtained from Temporal Difference Reinforcement Learning and Deep Q-learning approaches. The effectiveness of integrating signal processing techniques with Deep Q-learning is also explored. The discussion focuses on evaluating control performance, stability, and computational efficiency across these methodologies.

5.1. Baseline Flow Simulation and Validation

This subsection focuses on the baseline flow simulation and its validation against experimental data. Figure 7 demonstrates the pressure coefficient (C_p) distribution along the airfoil surface against experimental data of Mallor et al. [47] at an angle of attack $\alpha = 14^\circ$, for a Reynolds number $Re = 4.0 \times 10^5$, which shows a satisfactory agreement. Furthermore, the dimensionless wake velocity profile at T.E. is compared with other experimental and numerical studies of Tabatabaei et al. [48] in Fig. 8. In this figure, U_e is the edge velocity of the wake. The results indicate that the present simulation follows the overall trend of the numerical and experimental data.

Since this study aims to investigate the stall condition, the rest of the paper is focused on $\alpha = 15^\circ$. Fig. 9 presents the velocity magnitude, turbulent kinetic energy, and vorticity magnitude contours in the wake region. According to Figs. 7 and 9a, the separation point is about $0.55c$. Estimating the flow separation point location is necessary to determine the actuator placement on the suction side. According to previous research of Ebrahimi and Hajipour [32], the actuator placement upstream of the separation point is more effective in mitigating the flow separation. Figs. 9b and 9c demonstrate two shear layers following the separation point and T.E., which is the basis of utilizing the dual-point excitation technique. Thus, the pressure side actuator is placed on the airfoil's trailing edge.

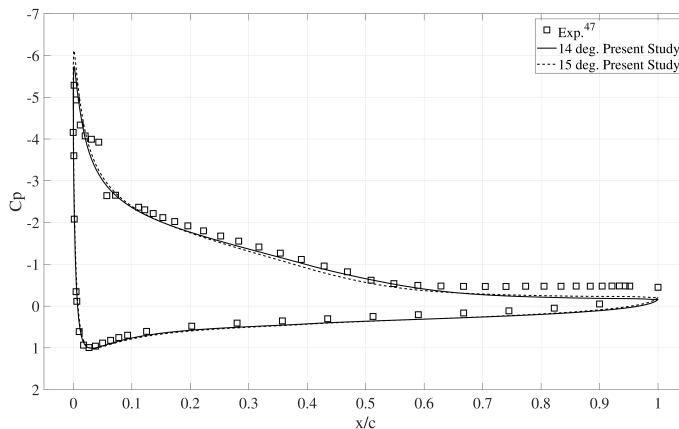


Figure 7: Comparison of C_p distribution along the x/c between experimental and CFD data.

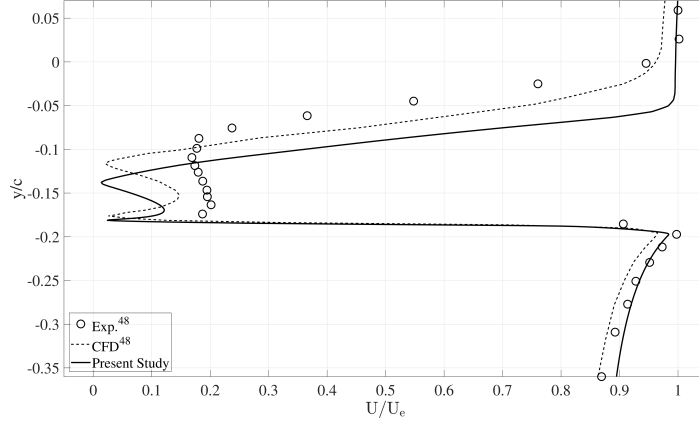


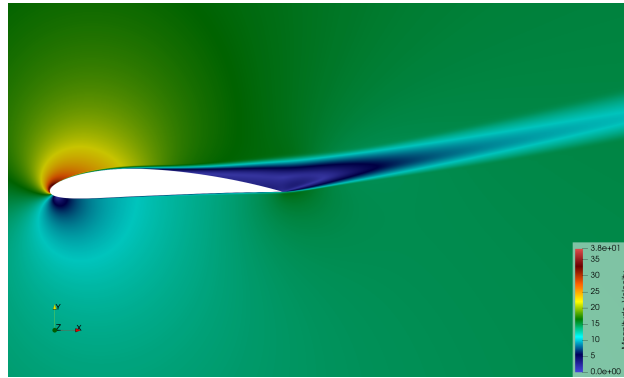
Figure 8: Comparison of wake velocity profiles at T.E.

This baseline flow physics is a reference point for determining and evaluating the performance of various control strategies. Under baseline conditions, the lift coefficient (C_l) and drag coefficient (C_d) have been calculated as $C_l = 1.44$ and $C_d = 0.045$, respectively. These values provide a quantitative measure of the aerodynamic performance of the airfoil in the absence of active control strategies.

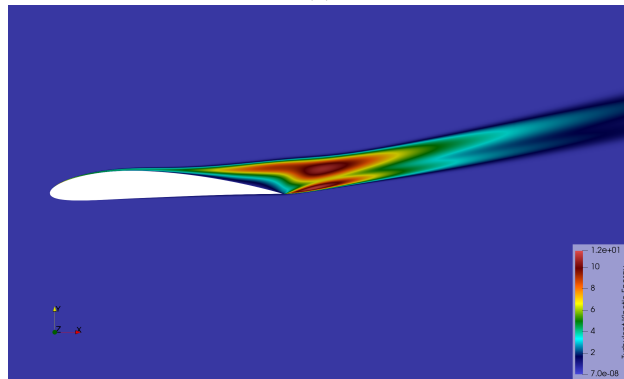
5.2. Adaptive MPC

The adaptive MPC was evaluated across two target values to assess its effectiveness in controlling flow separation. The analysis highlights the control strategy’s adaptability and impact on system stability and performance. First, a target C_l of 1.6 was selected as the desired output. The objective was to adjust the excitation frequency of the plasma actuators in real time to achieve and maintain this lift coefficient. The control system dynamically responds to the airfoil’s transient aerodynamic characteristics to ensure that the C_l reaches and stabilizes around the desired value of 1.6.

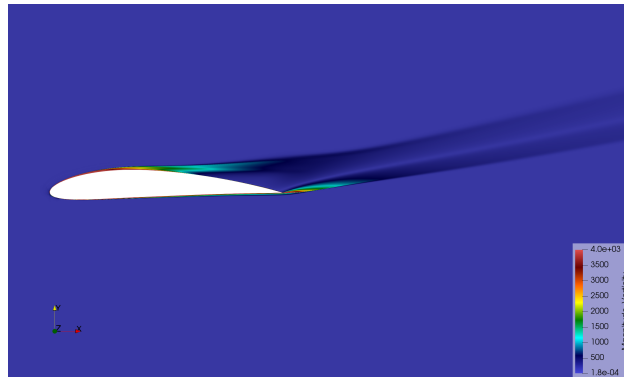
The provided graph, as shown in Fig. 10, illustrates the performance of the adaptive MPC system in achieving the desired lift coefficient. The top panel of the graph shows the time series of the C_l values along with its moving average. The bottom panel depicts the corresponding excitation frequencies applied during the control process. The lift coefficient was stabilized at around 2.8 s after activation of the controller.



(a)



(b)



(c)

Figure 9: Contours of baseline flow: (a) Velocity magnitude, (b) Turbulent kinetic energy, and (c) Vorticity magnitude.

To push the boundaries of the control system, aiming to achieve higher lift

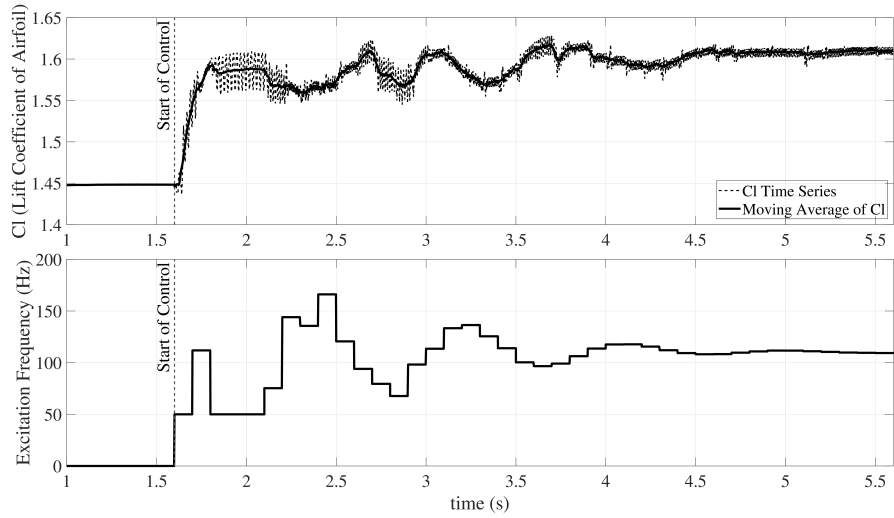


Figure 10: Desired C_l of 1.6 using adaptive MPC and its corresponding excitation frequencies.

coefficients, a second target C_l of 1.62 was selected. However, reaching such a high C_l presents significant challenges for the adaptive MPC to stabilize C_l around 1.62.

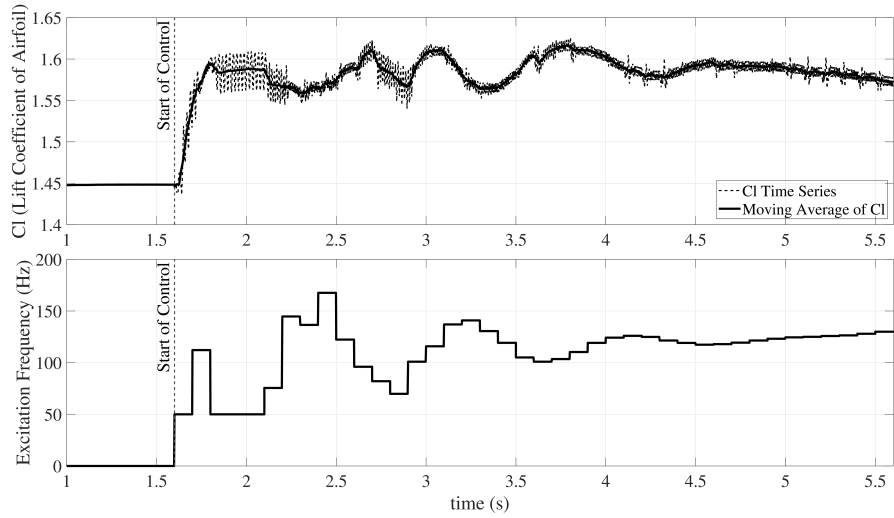


Figure 11: Desired C_l of 1.62 using Adaptive MPC and its corresponding excitation frequencies.

As depicted in Fig. 11, the controller could not stabilize the C_l at the desired value of 1.62. The fluctuations in the C_l time series indicate instability as the control system struggles to maintain the target value. This instability seems to arise because $C_l = 1.62$ is near the physical limit for the dual plasma actuator configuration, making it difficult for the controller to exert precise control. Consequently, the control system oscillates around the target, failing to maintain the given target.

5.3. TDRL

In contrast to the previous adaptive MPC approach, TDRL seeks to identify the optimal excitation frequency of plasma actuators that maximizes the C_l . Here, the action space is discrete, meaning the control system can only select from a predefined set of excitation frequencies. The goal is to explore these discrete actions to find the frequency that yields the highest C_l .

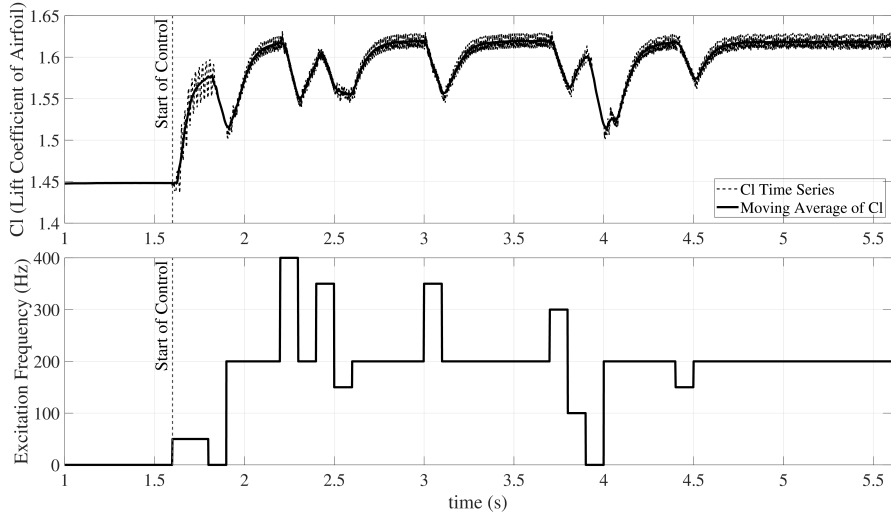


Figure 12: Exploring the optimal excitation frequency that maximizes C_l using TDRL.

Based on Fig. 12, the control system explored various frequencies before settling on 200 Hz as the optimal frequency for maximizing C_l . The top panel shows how C_l evolves over time, while the bottom panel depicts the selected excitation frequencies throughout the process. By the end of the simulation, the system determined that 200 Hz was the most effective frequency for achieving the maximum C_l . Notably, after four decision-makings, the controller found the optimal frequency of 200 Hz, resulting in a mean C_l of approximately 1.619.

5.4. DQL

The DQL approach's control system is designed to learn the optimal policy for selecting excitation frequencies that maximize the C_l . Unlike the previous TDRL, DQL utilizes a neural network to estimate the Q-values for each action, enabling the system to make more informed decisions in complex environments. The action space remains discrete, and the system learns by exploring different excitation frequencies and updating its policy based on the observed outcomes.

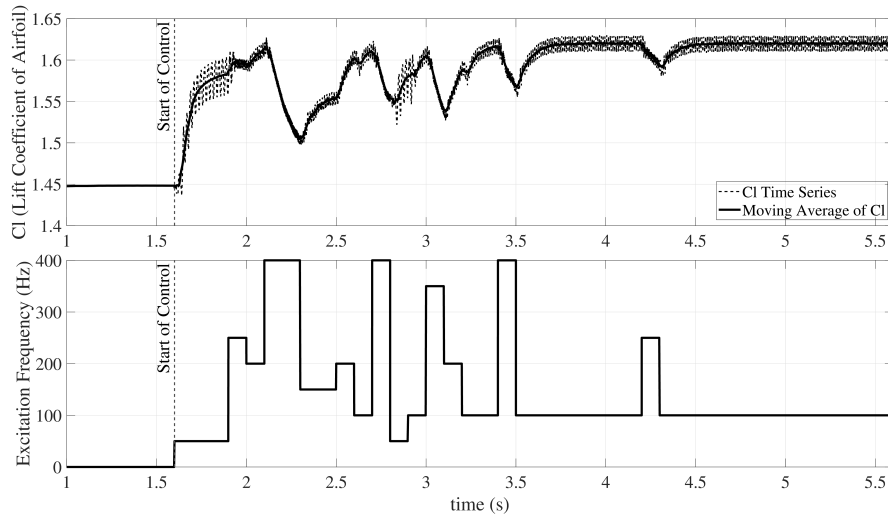


Figure 13: Selection of the optimal excitation frequency for maximizing C_l using DQL.

As shown in Fig. 13, the DQL algorithm explored various frequencies before selecting 100 Hz as the optimal excitation frequency. Despite the fluctuations during the learning phase, the system eventually converged to 100 Hz as the most effective frequency for achieving a high and stable C_l . After 11 decision makings, the controller found the optimal frequency of 100 Hz, resulting in a mean C_l of approximately 1.619.

5.5. Signal processing integrated with DQL

In this approach, DQL was enhanced by integrating signal processing techniques to improve the accuracy and robustness of the excitation frequency selection process. The objective was to refine the control system's ability to identify the optimal frequency for maximizing the lift coefficient. The system eventually selected 200 Hz as the optimal frequency. After 21

decision makings, the controller found the optimal frequency of 200 Hz, resulting in a mean C_l of approximately 1.619.

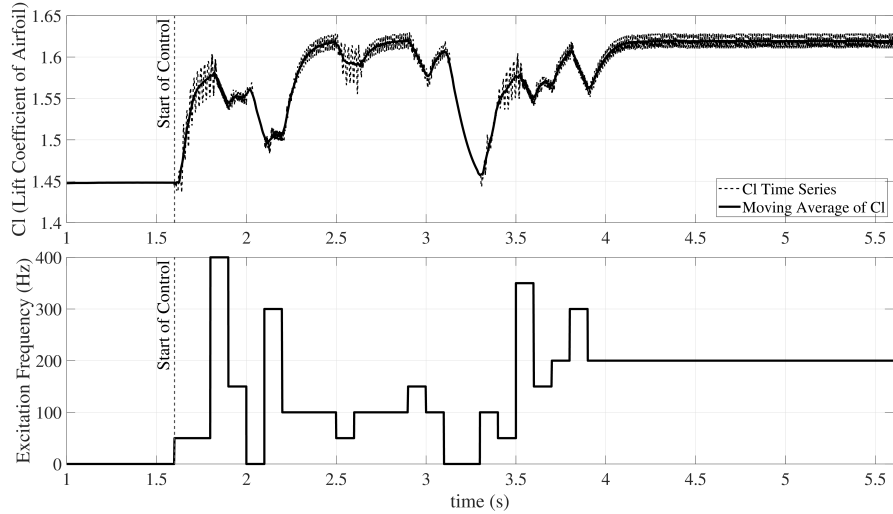


Figure 14: Selection of the optimal excitation frequency for maximizing C_l using signal processing integrated with DQL.

The average C_l for 100 Hz and 200 Hz are nearly identical, which made the decision-making process challenging for the network. The reason they are similar can be seen in the Fig. 15. For 100 Hz, there is one period of “on” and “off” states, while for 200 Hz, there are two periods. However, the first “on” phase for 200 Hz has a lower maximum than the “on” phase for 100 Hz, and the second “on” phase for 200 Hz reaches a higher maximum than 100 Hz. As a result, the average of the “on” states for 200 Hz becomes nearly identical to that of 100 Hz. This behavior suggests that the DQL produces similar average C_l compared to the signal processing integrated with DQL and TDRL cases, making it harder for the network to differentiate between the two based purely on C_l values.

5.6. Comparative Analysis

In this section, we compare different control strategies applied to the problem of flow separation control over a static airfoil at a near-stall angle of attack condition. Based on the algorithms discussed, the complexity level of the RL-based methods increases in the following order: TDRL, DQL, and

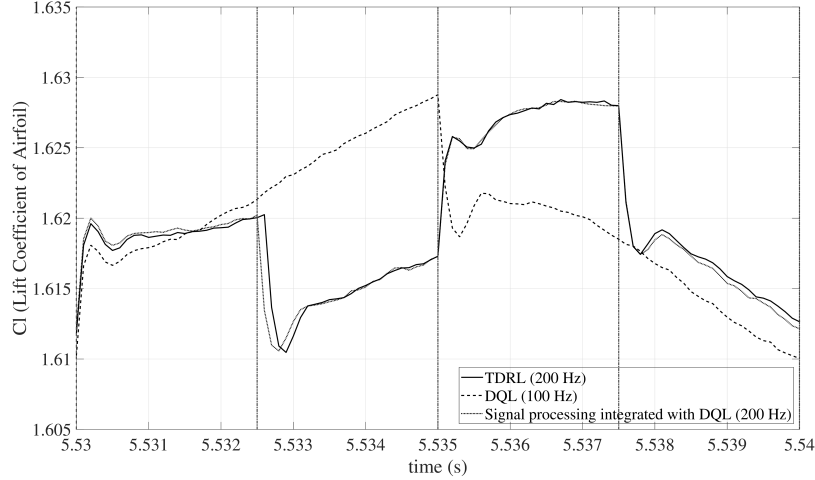


Figure 15: Comparison of results from different reinforcement learning methods for determining C_l

signal processing integrated with DQL. As the complexity of RL-based methods increases, they require more decision-making steps for accurate system identification.

As demonstrated in Fig.16, the time needed to achieve stability is reduced despite the higher number of decisions required by more complex methods. Also, it is observed that all RL-based methods successfully converge to an optimal C_l , albeit with different choices of actuation frequencies, achieving similar final values. In the case of the adaptive MPC approach, targeting a lift coefficient of 1.6, the actuator frequency stabilized around the excitation frequency of 110 Hz, which corresponds to $F^+ \approx 3$. The chosen target lift coefficient in the MPC method is close to the optimal value identified by RL-based methods, leading to an excitation frequency similar to that achieved by the DQL method (i.e., 100 Hz). This indicates that despite the differences in approach, there is a convergence in the key parameters, particularly in excitation frequency, between the adaptive MPC and RL-based methods.

To compare the controlled flow field with the baseline flow (as shown in Fig.9), Fig.17 presents the contours of velocity magnitude, turbulent kinetic energy, and vorticity magnitude. These results are specifically provided for the signal processing integrated with DQL method. Since the flow fields for other control methods are similar, their contours are not presented. This

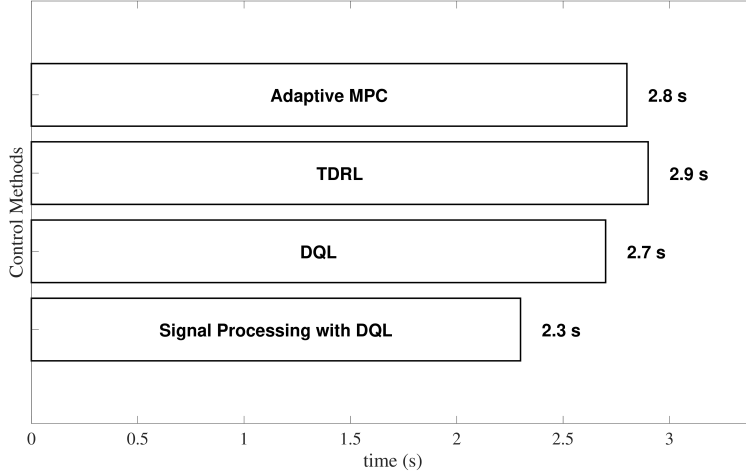
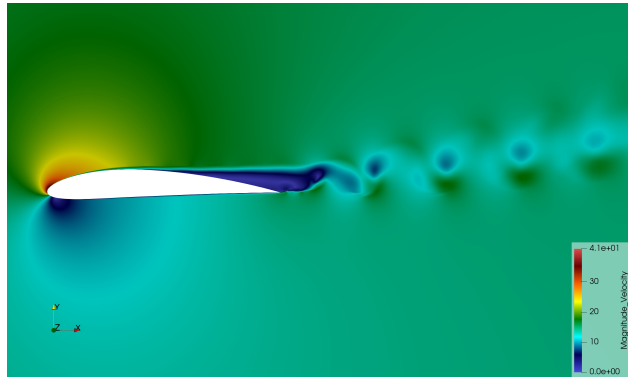


Figure 16: Stabilization time of different control methods.

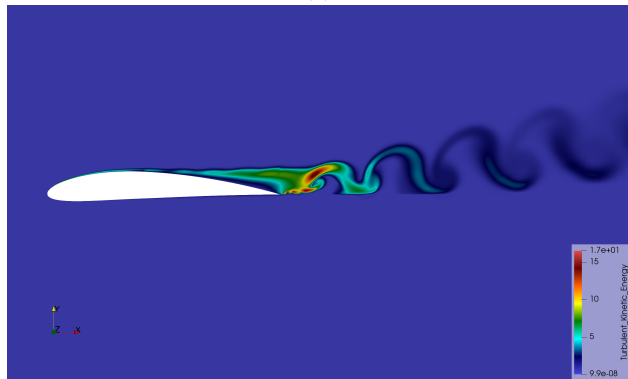
figure demonstrates that the proposed algorithms have successfully modified the flow field, including shear layers, wake, and separation points, compared to the baseline case. The velocity magnitude contours in Figures 9a and 17a reveal a reduction in the extent of the separation zone under the influence of the flow control method. This is further supported by the notable reduction in turbulent kinetic energy levels observed in the controlled case relative to the baseline flow (Figures 9b and 17b). Additionally, the vorticity magnitude contours in Figures 9c and 17c indicate that the separated shear layer on the airfoil’s suction side is inclined closer to the airfoil surface compared to the baseline case.

6. Conclusions

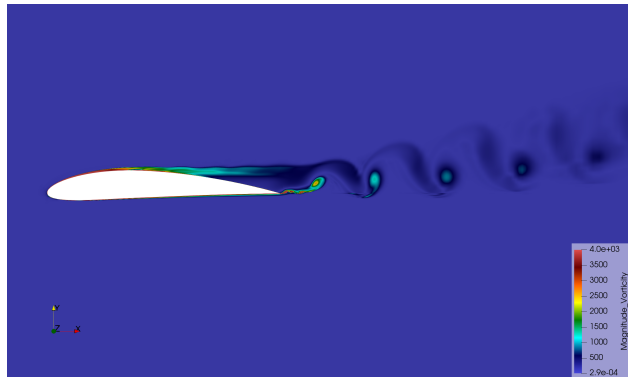
In this study, we explored various advanced control strategies for optimizing the aerodynamic performance of an airfoil by managing flow separation using plasma actuators. The concept previously introduced by the authors, dual-point excitation, is utilized to simultaneously excite both the suction side and trailing-edge shear layers using DBD plasma actuators. The applied control methods include adaptive MPC, TDRL, DQL, and integrated signal processing with the DQL method. These techniques were assessed based on their ability to stabilize the lift coefficient at targeted values under different operating conditions. Our findings revealed significant insights into



(a)



(b)



(c)

Figure 17: Contours of controlled flow using signal processing integrated with DQL method: (a) Velocity magnitude, (b) Turbulent kinetic energy, and (c) Vorticity magnitude.

the effectiveness and limitations of these methods in a highly dynamic and non-linear environment. The main findings are summarized as follows:

- **Adaptive MPC Performance:**

- The adaptive MPC approach effectively achieved the desired lift coefficient, C_l , of 1.60 when operating within the system’s physical limitations.
- Instabilities were observed when attempting to push C_l towards the upper physical limits, highlighting challenges in controlling the system near the actuator’s maximum capacity.
- While adaptive MPC is effective for moderate targets, its performance may deteriorate when extreme precision and control are required in more demanding situations.

- **RL-Based Methods:**

- RL-based methods, including TDRL, DQL, and DQL integrated with signal processing, demonstrated effective selection of excitation frequencies for maximizing C_l .
- Difficulty was noted in distinguishing between the optimal value of two excitation frequencies (100 Hz and 200 Hz) due to near-identical C_l values achieved at these frequencies.

- **Convergence and Frequency Observations:**

- The time required to achieve C_l value convergence is reduced despite the higher number of decisions necessitated by more complex methods.
- All RL-based methods successfully converged to an optimal C_l , albeit with different excitation frequencies.
- The adaptive MPC approach stabilized at an actuator frequency of approximately 110 Hz ($F^+ \approx 3$) for a target C_l of 1.6, aligning closely with the excitation frequency identified by the DQL method.
- There is a convergence in key parameters, such as excitation frequency, between adaptive MPC and RL-based methods, underscoring the alignment of both approaches in determining effective actuation strategies.

Future work could improve turbulence modeling and enhance the control system's ability to detect subtle frequency effects, potentially leading to more precise and effective flow control strategies. Additionally, incorporating the pitch and plunge motions of the airfoil could provide a basis for more complex aerodynamic problems to evaluate these control techniques.

Data Availability Statement

The data that support the findings of this study are available from the corresponding author upon reasonable request.

References

- [1] Z. Liu, L. Zhou, H. Tang, Z. Wang, F. Zhao, X. Ji, H. Zhang, Primary instability, sensitivity and active control of flow past two tandem circular cylinders, *Ocean Engineering* 294 (2024) 116863.
- [2] H. Ding, Z. Cheng, M. Liu, L. Xiao, S. Zhu, Effects of synthetic jet control parameters on characteristics of flow around a square cylinder at subcritical reynolds number, *Ocean Engineering* 309 (2024) 118577.
- [3] A. Seifert, A. Darabi, I. Wyganski, Delay of airfoil stall by periodic excitation, *Journal of aircraft* 33 (4) (1996) 691–698.
- [4] M. N. Sudin, M. A. Abdullah, S. A. Shamsuddin, F. R. Ramli, M. M. Tahir, Review of research on vehicles aerodynamic drag reduction methods, *International Journal of Mechanical and Mechatronics Engineering* 14 (02) (2014) 37–47.
- [5] J. L. Proctor, S. L. Brunton, J. N. Kutz, Dynamic mode decomposition with control, *SIAM Journal on Applied Dynamical Systems* 15 (1) (2016) 142–161.
- [6] N. Dovetta, P. J. Schmid, D. Sipp, Uncertainty propagation in model extraction by system identification and its implication for control design, *Journal of Fluid Mechanics* 791 (2016) 214–236.
- [7] S.-C. Huang, J. Kim, Control and system identification of a separated flow, *Physics of Fluids* 20 (10) (2008).

- [8] S. Obeid, G. Ahmadi, R. Jha, Narmax identification based closed-loop control of flow separation over naca 0015 airfoil, *Fluids* 5 (3) (2020) 100.
- [9] Y. Mao, S. Zhong, H. Yin, Model-based deep reinforcement learning for active control of flow around a circular cylinder using action-informed episode-based neural ordinary differential equations, *Physics of Fluids* 36 (8) (2024).
- [10] K. Portal-Porras, U. Fernandez-Gamiz, E. Zulueta, R. Garcia-Fernandez, S. E. Berrizbeitia, Active flow control on airfoils by reinforcement learning, *Ocean Engineering* 287 (2023) 115775.
- [11] C. Vignon, J. Rabault, R. Vinuesa, Recent advances in applying deep reinforcement learning for flow control: Perspectives and future directions, *Physics of fluids* 35 (3) (2023).
- [12] S. Shimomura, S. Sekimoto, A. Oyama, K. Fujii, H. Nishida, Closed-loop flow separation control using the deep q network over airfoil, *AIAA Journal* 58 (10) (2020) 4260–4270.
- [13] R. Paris, S. Beneddine, J. Dandois, Reinforcement-learning-based actuator selection method for active flow control, *Journal of Fluid Mechanics* 955 (2023) A8.
- [14] R. Vinuesa, O. Lehmkuhl, A. Lozano-Durán, J. Rabault, Flow control in wings and discovery of novel approaches via deep reinforcement learning, *Fluids* 7 (2) (2022) 62.
- [15] P. Varela, P. Suárez, F. Alcántara-Ávila, A. Miró, J. Rabault, B. Font, L. M. García-Cuevas, O. Lehmkuhl, R. Vinuesa, Deep reinforcement learning for flow control exploits different physics for increasing reynolds number regimes, in: *Actuators*, Vol. 11, MDPI, 2022, p. 359.
- [16] F. Ren, J. Rabault, H. Tang, Applying deep reinforcement learning to active flow control in weakly turbulent conditions, *Physics of Fluids* 33 (3) (2021).
- [17] W. Jia, H. Xu, Robust and adaptive deep reinforcement learning for enhancing flow control around a square cylinder with varying reynolds numbers, *Physics of Fluids* 36 (5) (2024).

- [18] B. Font, F. Alcántara-Ávila, J. Rabault, R. Vinuesa, O. Lehmkuhl, Active flow control of a turbulent separation bubble through deep reinforcement learning, in: *Journal of Physics: Conference Series*, Vol. 2753, IOP Publishing, 2024, p. 012022.
- [19] B. Font, F. Alcántara-Ávila, J. Rabault, R. Vinuesa, O. Lehmkuhl, Deep reinforcement learning for active flow control in a turbulent separation bubble (2024).
- [20] T. C. Corke, C. L. Enloe, S. P. Wilkinson, Dielectric barrier discharge plasma actuators for flow control, *Annual review of fluid mechanics* 42 (1) (2010) 505–529.
- [21] S. Oveisi, M. Mani, B. Mojarrad, M. Kazemi, Experimental investigation into the flow structure of plasma induced jet in a 2-d cross-flow, *European Journal of Mechanics-B/Fluids* 98 (2023) 102–119.
- [22] A. Ebrahimi, M. Hajipour, K. Ghamkhar, Experimental study of stall control over an airfoil with dual excitation of separated shear layers, *Aerospace Science and Technology* 82 (2018) 402–411.
- [23] B. Li, X. Meng, S. Yin, W. Hui, H. Li, Flow separation control over an airfoil using plasma co-flow jet, *AIAA Journal* 60 (4) (2022) 2195–2206.
- [24] M. Samimy, N. Webb, A. Esfahani, Reinventing the wheel: excitation of flow instabilities for active flow control using plasma actuators, *Journal of Physics D: Applied Physics* 52 (35) (2019) 354002.
- [25] A. Gross, H. Fasel, Active flow control for naca 6-series airfoil at $re=64,200$, *AIAA journal* 48 (9) (2010) 1889–1902.
- [26] T. C. Corke, M. L. Post, D. M. Orlov, Single dielectric barrier discharge plasma enhanced aerodynamics: physics, modeling and applications, *Experiments in Fluids* 46 (2009) 1–26.
- [27] A. Darabi, I. Wygnanski, Active management of naturally separated flow over a solid surface. part 1. the forced reattachment process, *Journal of Fluid Mechanics* 510 (2004) 105–129.
- [28] C. He, T. C. Corke, M. P. Patel, Plasma flaps and slats: an application of weakly ionized plasma actuators, *Journal of aircraft* 46 (3) (2009) 864–873.

- [29] T. Ashcraft, K. Decker, J. C. Little, Control of boundary layer separation and the wake of an airfoil using ns-dbd plasma actuators, in: 54th AIAA Aerospace Sciences Meeting, 2016, p. 0839.
- [30] M. Sato, H. Aono, A. Yakeno, T. Nonomura, K. Fujii, K. Okada, K. Asada, Multifactorial effects of operating conditions of dielectric-barrier-discharge plasma actuator on laminar-separated-flow control, *AIAA journal* 53 (9) (2015) 2544–2559.
- [31] M. Hajipour, A. Ebrahimi, X. Amandolese, Active flow control of a wing section in stall flutter by dielectric barrier discharge plasma actuators, *Physics of Fluids* 34 (7) (2022).
- [32] A. Ebrahimi, M. Hajipour, Flow separation control over an airfoil using dual excitation of dbd plasma actuators, *Aerospace Science and Technology* 79 (2018) 658–668.
- [33] F. Menter, Y. Egorov, A scale adaptive simulation model using two-equation models, in: 43rd AIAA aerospace sciences meeting and exhibit, 2005, p. 1095.
- [34] W. Shyy, B. Jayaraman, A. Andersson, Modeling of glow discharge-induced fluid dynamics, *Journal of applied physics* 92 (11) (2002) 6434–6443.
- [35] I. Maden, R. Maduta, J. Kriegseis, S. Jakirlić, C. Schwarz, S. Grundmann, C. Tropea, Experimental and computational study of the flow induced by a plasma actuator, *International Journal of Heat and Fluid Flow* 41 (2013) 80–89.
- [36] Z. Li, B. Hu, S. Lan, J. Zhang, J. Huang, Control of turbulent channel flow using a plasma-based body force, *Computers & fluids* 119 (2015) 26–36.
- [37] C. M. Rhie, W.-L. Chow, Numerical study of the turbulent flow past an airfoil with trailing edge separation, *AIAA journal* 21 (11) (1983) 1525–1532.
- [38] S. J. Qin, T. A. Badgwell, A survey of industrial model predictive control technology, *Control engineering practice* 11 (7) (2003) 733–764.

- [39] M. Morari, J. H. Lee, Model predictive control: past, present and future, *Computers & chemical engineering* 23 (4-5) (1999) 667–682.
- [40] J. M. Maciejowski, M. Huzmezan, Predictive control, in: *Robust Flight Control: A Design Challenge*, Springer, 2007, pp. 125–134.
- [41] E. Fernandez-Camacho, C. Bordons-Alba, *Model predictive control in the process industry*, Springer, 1995.
- [42] E. F. Camacho, C. Bordons, E. F. Camacho, C. Bordons, *Constrained model predictive control*, Springer, 2007.
- [43] D. W. Clarke, C. Mohtadi, P. S. Tuffs, Generalized predictive control—part i. the basic algorithm, *Automatica* 23 (2) (1987) 137–148.
- [44] R. E. Kalman, A new approach to linear filtering and prediction problems (1960).
- [45] V. Mnih, K. Kavukcuoglu, D. Silver, A. A. Rusu, J. Veness, M. G. Bellemare, A. Graves, M. Riedmiller, A. K. Fidjeland, G. Ostrovski, et al., Human-level control through deep reinforcement learning, *nature* 518 (7540) (2015) 529–533.
- [46] J. Schmidhuber, S. Hochreiter, et al., Long short-term memory, *Neural Comput* 9 (8) (1997) 1735–1780.
- [47] F. Mallor, C. S. Vila, M. Hajipour, R. Vinuesa, P. Schlatter, R. Örlü, Experimental characterization of turbulent boundary layers around a naca 4412 wing profile, *Experimental Thermal and Fluid Science* (2024) 111327.
- [48] N. Tabatabaei, M. Hajipour, F. Mallor, R. Örlü, R. Vinuesa, P. Schlatter, Rans modelling of a naca4412 wake using wind tunnel measurements, *Fluids* 7 (5) (2022) 153.